Atmospheric Influence upon Crystallization and Electronic Disorder and Its Impact on the Photophysical Properties of Organic–Inorganic Perovskite Solar Cells

Sandeep Pathak,[*,†,‡] **Alessandro Sepe,**[‡] **Aditya Sadhanala,**[‡] **Felix Deschler,**[‡] **Amir Haghighirad,**[†] **Nobuya Sakai,**[†] **Karl C. Goedel,**[‡] **Samuel D. Stranks,**[†] **Nakita Noel,**[†] **Michael Price,**[‡] **Sven Hüttner,**[‡] **Nicholas A. Hawkins,**[§] **Richard H. Friend,**[‡] **Ullrich Steiner,**[*,⊥] **and Henry J. Snaith**[*,†]

[†]Clarendon Laboratory, Department of Physics, University of Oxford, Parks Road, Oxford OX1 3PU, United Kingdom, [‡]Cavendish Laboratory, Department of Physics, University of Cambridge, 19 JJ Thomson Avenue, Cambridge CB3 0HE, United Kingdom, [§]Oxford Silk Group, Department of Zoology, University of Oxford, South Parks Road, Oxford OX1 3PS, United Kingdom, and [⊥]Adolphe Merkle Institute, Chemin des Verdiers, CH-1700, Fribourg, Switzerland

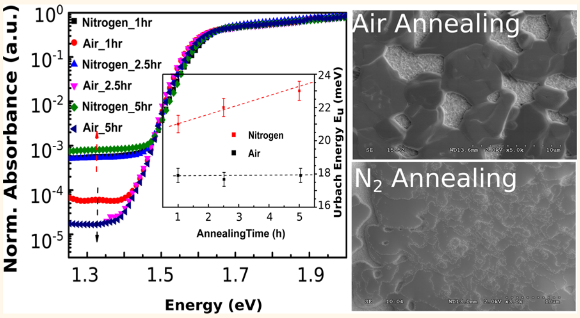

ABSTRACT Recently, solution-processable organic–inorganic metal halide perovskites have come to the fore as a result of their high power-conversion efficiencies (PCE) in photovoltaics, exceeding 17%. To attain reproducibility in the performance, one of the critical factors is the processing conditions of the perovskite film, which directly influences the photophysical properties and hence the device performance. Here we study the effect of annealing parameters on the crystal structure of the perovskite films and correlate these changes with its photophysical properties. We find that the crystal formation is kinetically driven by the annealing atmosphere, time and temperature. Annealing in air produces an improved crystallinity and large grain domains as compared to nitrogen. Lower photoluminescence quantum efficiency (PLQE) and shorter photoluminescence (PL) lifetimes are observed for nitrogen annealed perovskite films as compared to the air-annealed counterparts. We note that the limiting nonradiative pathways (*i.e.*, maximizing PLQE) is important for obtaining the highest device efficiency. This indicates a critical impact of the atmosphere upon crystallization and the ultimate device performance.

KEYWORDS: photovoltaic · perovskite solar cell · thermal annealing · crystal symmetry · electronic disorder · organic–inorganic

Generating cost-effective and environmentally benign renewable energy remains a major challenge for scientific and technological development.[1] On the basis of a broad range of materials,[2–5] organic photovoltaic (OPV), dye-sensitized solar cells (DSSCs), chalcogenide quantum dots[6] and semiconductor-sensitized extremely thin absorber solar cells[7–9] are some of the most promising technologies for low-cost manufacture of solution-processed photovoltaic. These devices are, however, limited in their performance typically due to a complex design and limited exciton and charge carrier diffusion lengths.[7,9,10] A recent revolutionary breakthrough is the solution processed organic–inorganic metal halide perovskite-based solar cells, with power conversion efficiencies exceeding 17%[11–17] consisting of the ABX_3 ($A = CH_3NH_3^+$; $B = Pb^{2+}$; and $X = Cl^-, I^-$, and Br^-).[18,19] The main attributes of $CH_3NH_3PbX_3$ ($MAPbX_3$) are its strong light absorption,[12,16,20–22] long charge carrier lifetime (exceeding 300 ns),[21] diffusion lengths (exceeding 1 μm for electrons and holes),[21,23,24] photoluminescence quantum efficiency (PLQE) as high as 70%[25] and its ambipolar charge transport capabilities.[12,16,20] These allow efficient light harvesting and charge collection across the entire thickness of the perovskite layer (typically 400 nm), making it highly efficient.[22] Exhibition of such extraordinary optical and electronic properties can mainly be attributed to

* Address correspondence to
sandeep.pathak@physics.ox.ac.uk,
ullrich.steiner@unifr.ch,
h.snaith1@physics.ox.ac.uk.

Received for review November 12, 2014
and accepted February 24, 2015.

10.1021/nn506465n

their highly crystalline frameworks with a precise high symmetry crystal structure.[22,26−29] Despite the enormous advances in device performance and the basic understanding of perovskite crystal structure formation, the influence of processing conditions on perovskite crystal structure is still unknown. From a structural point of view, $CH_3NH_3PbX_3$ (X = I, Cl) perovskites that utilize a mixed iodide/chloride precursor combination (CH_3NH_3I and $PbCl_2$), herein termed "mixed halide perovskite", reportedly have a tetragonal structure at room temperature similar to the $CH_3NH_3PbI_3$ perovskite.[20] For the $CH_3NH_3PbI_2Br$ system, tetragonal and cubic phases have been proposed based on XRD data.[26,30] Baikie *et al.* have highlighted the reversible phase transition from tetragonal to cubic symmetry above 56 °C in bulk $CH_3NH_3PbI_3$ perovskite;[31] however, no such observation has been made so far in the thin film. Hence the annealing conditions could be the key to control the crystal symmetry of the perovskite.[31,32] A greater understanding of the crystal structure and its implications on photoconversion mechanisms will pave the way for better reproducibility of device performance and to rationally modify and tailor crystal parameters for higher efficiencies.

In this article, we investigate the influence of annealing atmosphere (*i.e.*, air and nitrogen) and time on isothermal (100 °C) annealing of perovskite films deposited from the mixed halide precursor (*i.e.*, $3CH_3NH_3I$: $1PbCl_2$). We find that the observed change in crystal structure and microstructural features correlate strongly with the photophysical properties of the perovskite and hence with device performance. This study helps in setting the agenda for further optimization of the crystal chemistry to achieve greater reproducibility and higher device performance.

RESULTS AND DISCUSSION

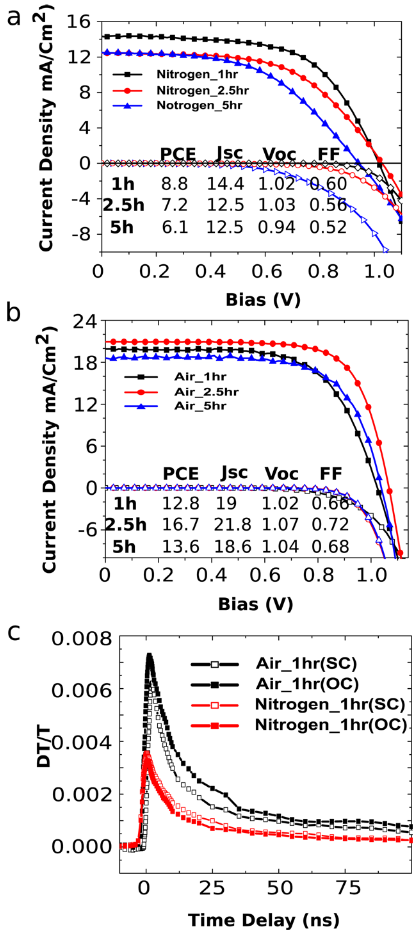

Figure 1. *J*−*V* curves recorded under AM 1.5 simulated sun light (100 mW cm^{-2}), with respective dark currents for devices, in which the perovskite layer was annealed for 1, 2.5, and 5 h at 100 °C under (a) nitrogen and (b) air. The PCE (%), Jsc (mA/cm^2), V_{oc} (V) and FF are shown in the inset. (c) Transient absorption kinetics of a bleach signal at 1.6 eV of perovskite-based devices with a spiro-OMeTAD hole acceptor layer prepared under air and nitrogen atmosphere for 1 h isothermal annealing. The devices were photoexcited at 2.33 eV (2 μJ/cm^2, pulse length 0.6 ns). Transient absorption measurements were performed in reflection geometry.

The precursor solution used here to deposit perovskite film contains $3CH_3NH_3I$: $1PbCl_2$ in DMF and properties studied do not stem from the "pure" $CH_3NH_3PbI_3$ (as obtained from the 1:1 reaction between PbI_2 and CH_3NH_3I) but only for the $CH_3NH_3PbI_{3-x}Cl_x$ /$2CH_3NH_3X$ (X = Cl/I mixture), as the extent of byproduct (*i.e.*, $2CH_3NH_3X$) removal during annealing is still under investigation. We fabricated solution-processed meso-superstructure solar cells (MSSCs) with the mixed halide perovskite, $CH_3NH_3PbI_{3-x}Cl_x$, as discussed elsewhere.[12] The porous meso-structured Al_2O_3 scaffold on fluorine-doped tin oxide (FTO)-coated glass substrates, coated with an n-type TiO_2 compact layer, was filled with the perovskite, and in addition giving a solid perovskite capping layer of ∼200 nm. During the process of film fabrication, the samples were annealed isothermally at 100 °C in different atmospheres, *i.e.*, air (humidity 40%) and nitrogen, for 1, 2.5, and 5 h. Subsequently, p-type spiro-OMeTAD was deposited as a hole-transporting layer so as to form a p-i-n (TiO_2-perovskite-spiro-OMeTAD) heterojunction architecture.[33] Current−voltage characteristics measured under simulated AM1.5 100 mW cm^{-2} sun light for the best devices fabricated are shown in Figure 1a and b. The performance parameters for a larger batch of devices are shown in Figure S1 (Supporting Information). While annealing in air, we observe no substantial variation in J_{sc} for 1, 2.5, and 5 h of annealing; however, the FF and V_{oc} increase from 1 h to 2.5 h annealing but then deteriorated when annealed further to 5 h. The 2.5 h annealing produces the highest PCE of 16.7% as compared to 1 h (12.8%) and 5 h (13.6%) annealed samples. Upon annealing in nitrogen atmosphere (*i.e.*, in glovebox), however, the device performance was much lower, mainly due to a reduced short circuit current and fill-factor. Longer time annealing under nitrogen for 2.5 and 5 h further deteriorated the device performance. After 5 h annealing in nitrogen atmosphere we observe that the power conversion efficiency has halved in comparison to the samples annealed in air. In Figure S2 we show anomalous hysteresis in the current–voltage curves measured from forward bias to short circuit (scan 1) and from short circuit to forward bias (scan 2) under simulated 1.5 AM (100 mW cm-2) sun light for; (top panel) air annealed perovskite and (bottom panel) for nitrogen annealed samples. Hysteresis in $J-V$ curves appears to be higher for sample annealed under nitrogen atmosphere as compared with the air annealed samples. Annealing time does not appear to be influencing the hysteresis in $J-V$ curve too much. The hysteresis in the perovskite solar cell performance may originate either from the charge collection interfaces or from the ion migration in the bulk material or from both.[34]

To estimate the charge carrier population and recombination of these devices, we performed transient absorption experiments under working conditions for samples that were annealed for 1 h either in nitrogen or in air. Figure 1c shows the transient absorption kinetics of the dominant bleach signal at 1.6 eV, which scales with the photogenerated charge population in the working devices at open-circuit. For the devices with air-annealed perovskite layers, the initial bleach signal was higher by a factor of 2 compared to nitrogen-annealed devices, indicating a higher number of photogenerated charges for the air-annealed devices. Note that the TA bleach signal is corrected for respective absorption. The decay time of the bleach signal in nitrogen-annealed devices ($\tau_{1/2}$ = 9.4 ns) was slightly faster compared to air-annealing ($\tau_{1/2}$ = 11.3 ns). This suggests a faster recombination in nitrogen-annealed devices, hindering charge extraction. We do note that these intensities are higher than those under standard solar cell operation.

These findings show two shortcomings in charge generation and recombination in nitrogen-annealed perovskite devices, which are critical for efficient device performance, and they correlate with the difference in their photoconversion efficiencies. The differences in spectroscopic response of the perovskite layers could be caused by variations in stoichiometry and crystallinity caused by the different processing environment or the interaction of the perovskite layers with their interfaces. In order to further understand the photophysical properties of perovskite films, steady state and time-resolved PL measurements were performed on isolated perovskite films (*i.e.*, with no p or n-type contact layers). The perovskite films were fabricated on glass substrates with similar annealing conditions as those discussed above. When annealed in nitrogen, the steady state PL results show a gradual reduction in intensity with increasing annealing time from 1 to 5 h, on the contrary when air annealed, we observe the highest PL intensity after 2.5 h of annealing and then further annealing up to 5 h leads to a reduction in PL intensity (Figure 2a). The steady state time integrated PL intensity is 1 order of magnitude higher in air-annealed samples compared to the nitrogen-annealed samples (Figure 2a). Interestingly, nitrogen-annealed samples show a red-shifted emission peak (1.56 eV) compared to films prepared under ambient conditions (1.59 eV), with a peak shift of ~20–30 meV. Further annealing for 2.5 and 5 h shows a further red shift in emission peak. This lower emission energy may indicate a higher electronic disorder in the film, allowing photoexcitations to relax to lower energetic states, or point toward a difference in crystal size/structure or due to a combined effect, giving rise to a different band-structure.[35] Annealing in air for up to 2.5 h does not show any detectable PL emission peak shift; however, a slight blue shift is observed when annealed for 5 h. Figure 2b shows the time-resolved PL decay for the perovskite films, with the longer decay for films prepared under ambient conditions ($\tau_{1/2}$ = 114, 120, and 50 ns for 1, 2.5, and 5 h, respectively), compared to the films prepared under nitrogen ($\tau_{1/2}$ = 70, 31, and 24 ns for 1, 2.5, and 5 h, respectively). The similar trend is also seen in the PLQE values, with a significantly higher value (22.4, 24.2, and 18.1% for 1, 2.5, and 5 h, respectively) for films prepared under ambient conditions compared to nitrogen annealed films, which demonstrate PLQE values lower than 20% (18.8, 10.2, and 8.3% for 1, 2.5, and 5 h, respectively). Extending dwelling time from 1 h to 5 h resulted in faster PL decays while annealing in nitrogen, in contrast with air annealing where it first increases peaking at 2.5 h of dwelling and then decreases again after 5 h of annealing. Expectedly, the PLQE value follows the similar trend with the varying dwelling time as the PL intensity and PL decay time. We summarize the PLQE and PL half-life values in Table 1.

An interesting observation is that the air annealed perovskite films show higher absorption in the visible region than the nitrogen-annealed film, a trend that is surprisingly reversed in the Near-IR region (Figure 2c). These observations indicate that a change in crystal symmetry is partially responsible for the observed red shift in PL emission and is not exclusively due to the energy relaxation.[28,30,31] A higher degree of crystal disorder could lead to lower PLQEs, PL lifetimes and higher recombination in nitrogen-annealed samples.

The photocurrent will be limited by diffusion length, and a longer PL lifetime suggests a longer diffusion length. The device photocurrents presented in the manuscript indeed scale roughly with PL lifetime. On the other hand, the V_{oc} will be limited by the presence of nonradiative recombination. On the basis of the ideal diode equation, the reciprocity relation between electroluminescent emission and photovoltaic quantum efficiency of solar cells developed

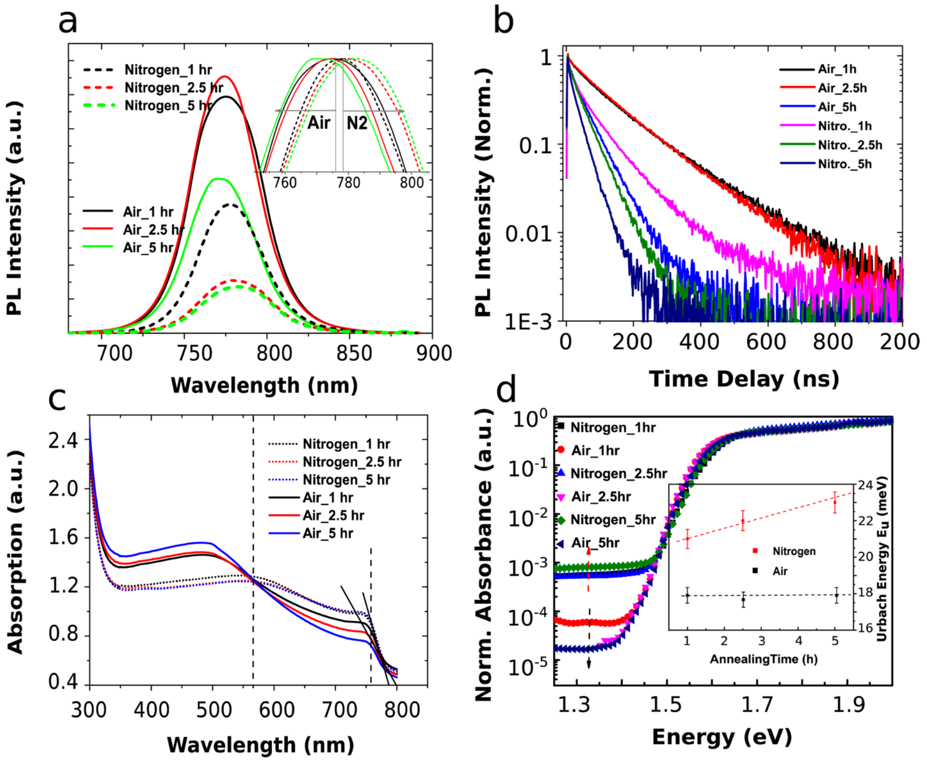

Figure 2. (a) Steady-state PL spectra of thin mixed halide perovskite films prepared under nitrogen and ambient conditions for different annealing times and temperatures. Photoexcitation was performed at 2.33 eV with a fluence of 0.5 mW/cm^2. (b) Time-resolved PL kinetics of mixed halide perovskite films on glass as a function of time delay after photoexcitation. The films were photoexcited using a 507 nm laser head pulsed at frequencies of 1 MHz and fluence of ~300 nJ/cm^2. (c) Linear absorption spectra for different annealing times and temperatures. (d) PDS spectra of air and nitrogen annealed perovskite films. The inset shows the Urbach energy for the samples.

TABLE 1. PLQE (with Standard Deviation), PL Half-Life, and Urbach Energy of the Perovskite Films Annealed in Different Conditions

annealing	time (h)	PLQE (%)	PL half-life (ns)	Urbach energy (meV)
air	1	22.4 ± 0.8	114	18
	2.5	24.2 ± 0.5	120	17.7
	5	18.1 ± 1.0	50	18.1
nitrogen	1	18.8 ± 0.8	70	21
	2.5	10.2 ± 1.1	31	22
	5	8.3 ± 1.0	24	23

by Rau *et al.*[36] is given by

$$qV_{oc} = k_BT \times \ln\left(\frac{\int_0^\infty \eta_{EQE}(\lambda)\phi_{ph}^{AM1.5}(\lambda)\,d\lambda}{\int_0^\infty \eta_{EQE}(\lambda)\phi_{ph}^{bb}(\lambda)\,d\lambda}\right) - k_BT \times |\ln \eta_{EL}|$$

The second term in the equation accounts for the loss in the V_{oc} due to the electroluminescence quantum efficiency (η_{EL}) being less than 1, *i.e.*, due to the presence of nonradiative pathways. The expression is logarithmic so changes in luminescence quantum efficiency (*i.e.*, PLQE) will only manifest itself in small changes in V_{oc}. Nevertheless, the voltage drop is evident for the long nitrogen-annealed sample, where the PLQE also substantially drops. Therefore, it is important to note that limiting nonradiative pathways (*i.e.*, maximizing PLQE) is important for obtaining the highest device efficiency.[37]

These measurements may therefore represent a fingerprint for differences in perovskite crystal structure induced by variations in the annealing conditions. To evaluate and quantify the overall degree of disorder induced by the varying annealing conditions we performed photothermal deflection spectroscopy (PDS)[38] on the perovskite films which we present in Figure 2d.

PDS can estimate the level of disorder in the perovskite by sensitively measuring the light absorption at the band edge and within the band gap; the absorption at the band edge characterizes the band-tail states induced by disorder in the crystal.[39] This sub-band gap absorption tail has an exponential variation, $A \sim \exp(E/E_u)$, defining the Urbach Energy E_u, which is a measure for the degree of disorder within the material.[40]

We show the calculated Urbach energies for the different perovskite films in the inset of Figure 2d and also summarized in Table 1, highlighting a clear trend in crystal disorder for the two annealing conditions. For all annealing times, air annealed samples exhibit remarkably lower level of disorder than nitrogen annealed. Increasing the dwelling time from 1, 2.5,

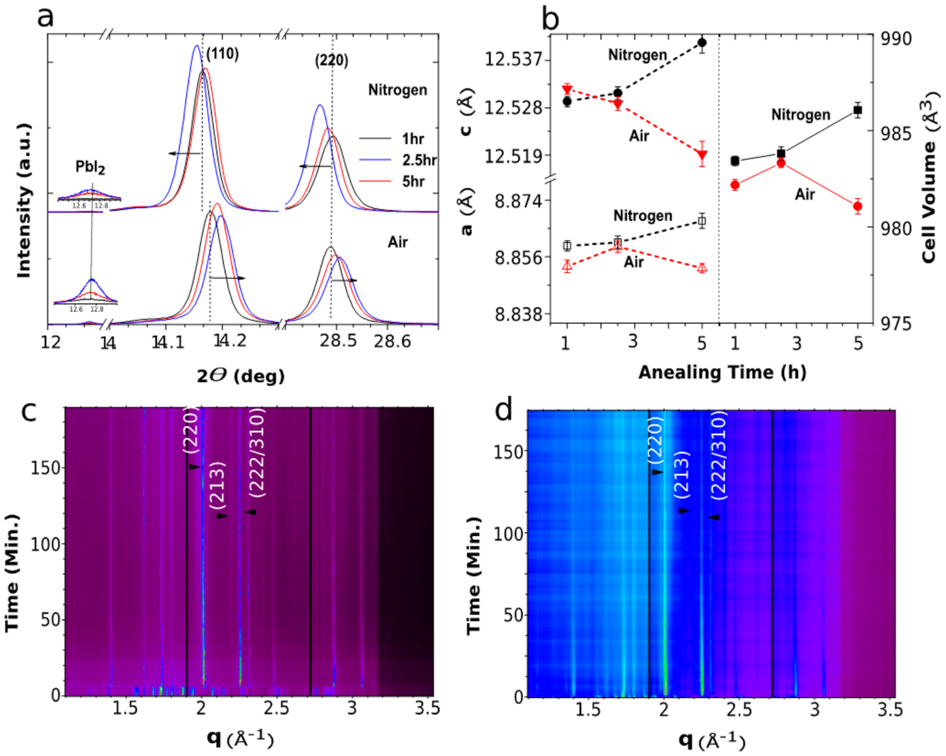

Figure 3. (a) X-ray diffraction pattern showing $(110)^{cub}$ and $(220)^{cub}$ Bragg reflections of $MAPbI_{3-x}Cl_x$ thin film annealed at different conditions. (b) Calculated lattice parameters by McMaille method of thin film X-ray diffraction spectrum. (c and d) Two-dimensional *in situ* WAXS image of bulk perovskite, annealed iso-thermally at 100 °C for 2.5 h in air (c) and nitrogen (d). The 2D images illustrate a defined $(213)^{tet}$ reflection annealed in air that confirms retaining of its crystallinity contrary to the samples annealed in nitrogen atmosphere.

and 5 h shows gradual increase in disorder level. However, there is little difference in the Urbach energies for 1, 2.5, and 5 h air annealed samples, which are within the error range of the fit used to extract the Urbach energy (± 0.5 eV).

To identify the origin of the disorder in the perovskite film we have performed structural studies on samples annealed in different atmospheres (*i.e.*, nitrogen and air) and dwelling times. The XRD patterns of perovskite thin film on glass slides are shown in Figure 3a. In thin films, due to a preferred orientation of crystallites, the predominant peaks which appear are assigned to cubic crystallographic planes $(110)^{cub}$, $(220)^{cub}$ and $(310)^{cub}$, as we show in Figure S3. We did not observe the reflections $(211)^{tet}$ and $(213)^{tet}$ reminiscent of the tetragonal structure consistent with a preferred orientation in the film. However, in the XRD patterns of bulk samples we do observe the reflections assigned to a tetragonal structure, as we show in Figure S4. To observe changes in the crystal structure during annealing, we mainly focus on two major reflections, *i.e.*, $(110)^{cub}$ and $(220)^{cub}$, (see Figure 3a).

Qualitatively, we observe two major differences in XRD patterns of perovskite films annealed in air and in nitrogen for 1 h. First, in samples annealed in air small amounts of PbI_2 are detected by XRD, while this was not seen in samples annealed in nitrogen for up to 2.5 h.

Second, the $(220)^{cub}$ reflection in the XRD lies at the same 2θ position (28.3°) for both air and nitrogen annealed films, this is in contrast to the $(110)^{cub}$ peak, which is shifted to lower 2θ value (from 14.7° to 14.6°) for nitrogen annealed perovskite films compared to air annealed samples (see Figure 3a). The shift in 2θ for nitrogen *vs* air-annealed samples is indicative of a change in the lattice parameters. Systematic peak shifts toward higher 2θ angle are observed for samples annealed in air for 2.5 and 5 h suggesting lattice contraction. On the contrary, annealing in nitrogen shows a systematic lattice expansion (peak shift toward lower 2θ angle) with increasing annealing time (2.5 and 5 h). However, the difference in lattice parameter becomes more pronounced only after 5 h of annealing in either atmosphere. In Figure 3b we present crystal lattice parameters and cell volume *vs* annealing time.

We have employed *in situ* wide-angle X-ray scattering (WAXS) on $CH_3NH_3PbI_{3-x}Cl_x$ perovskite films while annealing at 100 °C for 2.5 h to investigate the effect on crystallinity, phase formation and stability in both nitrogen and air atmosphere (Figure 3c and d). To perform this measurement we spin-coated the perovskite precursor solution on a glass slide and dried it at RT, the dried film was then scratched off the substrate to perform *in situ* WAX. We employed a wide *q*-range (Å) to map out the structural features that

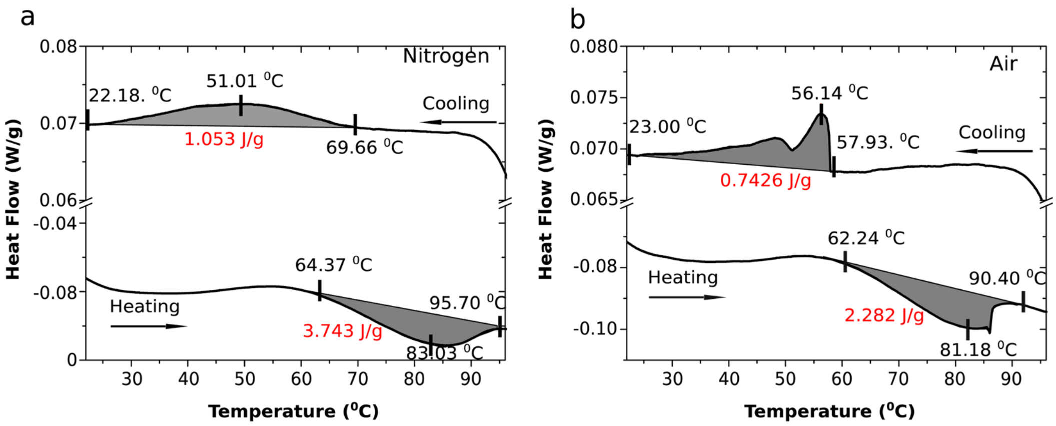

Figure 4. Differential scanning calorimetry (DSC) profile of bulk perovskite in air and nitrogen atmosphere showing a reversible tetragonal to cubic phase transition, (a) DSC profile of perovskite in nitrogen atmosphere showing a pronounced transition ranging over a large temperature range with an onset temperature of 51.01 °C. (b) A sluggish transition is observed in air, involving much less energy. Additionally, a majority of the transition appears to be occurring at ~56 °C.

appear during the annealing process. Annealing in air for up to 2.5 h has a negligible influence on the peak intensity and the crystallinity of the films, in contrast to annealing in nitrogen, where deterioration in the perovskite crystallinity is observed (Figure 3c and d). An interesting difference between the two sample is that under nitrogen atmosphere, perovskite crystals show smooth phase transition with the disappearance of $(211)^{tet}$ and $(213)^{tet}$ reflections, whereas annealing in air shows a resistance in phase transition under the studied annealing conditions. The different ratio of tetragonal and cubic phase could remain in the perovskite film due to the variation in the kinetics of phase transition in different conditions (Figure S5). To divulge the kinetics of the phase transition under varying atmosphere (air and nitrogen) we carried out differential scanning calorimetric (DSC) measurements of the bulk perovskite crystal. We show the DSC profile (heat flow *vs* temperature) during the heating and cooling process in air and in nitrogen in Figure 4 a and b.

As previously reported, the bulk perovskite crystal, at higher temperatures (327–330 K) the tetragonal $MAPbX_3$ perovskite ($I4/mcm$, NO. 140) reportedly becomes cubic ($Pm\overline{3}m$, No. 221), which is reversible when it is cooled down to room temperature[31] by titling the $[PbI_6]^{4-}$ octahedral along the crystallographic *c*-axis. The DSC profile confirms the reversible transition from tetragonal (RT) to cubic when heated above >62–64 °C and *vice versa* when cooled down to room temperature. The shaded area in the profile tells about the energy involved in transition, associated energy; transition and onset temperature for the said transition for each phase has been mentioned in the figure. In apparent hysteresis in transition confirms the first-order phase transition, which indicates toward a structural change in the perovskite crystal. The transition extends over a large temperature range and may retain fraction of cubic phase even after cooling to room temperature. In contrast to the nitrogen atmosphere, transition appears to be sluggish in air atmosphere and also the cooling profile is abrupt and strong at 56.14 °C indicating major transition at this point.

The reversibility of the phase transition from higher symmetry (cubic) to lower symmetry (tetragonal) would depend on the thermodynamic parameter (*i.e.*, temperature and/or pressure) as confirmed by the Figure 4a and b. Heating at 100 °C (>60 °C) may transform the otherwise tetragonal perovskite crystal to cubic at higher temperature and when the film is cooled quickly to room temperature the sudden transformation back from cubic to tetragonal may preserve a tetragonal–pseudocubic phase.[31] The difference in the kinetics of the phase transition while annealing in different atmosphere may give a different ratio of tetragonal–pseudocubic phase in the perovskite. It is note-worthy that the as observed phase-transition is in the bulk perovskite. Although, the observed phase transition in bulk perovskite crystal may not completely be implied (for instance due to preferred orientation) in the thin films, nevertheless, the induced strain in the film could well be originated from such phase transition (change in unit cell volume cubic compared to tetragonal). This, however, may explain the lattice expansion and contraction when annealed under nitrogen and air atmosphere, respectively. We first heat the sample (in nitrogen or air) for a stated dwell time and cooled it back to room temperature before measuring the XRD. The annealing time may influence the kinetics of the phase transition and have impact on the phase fraction cubic *vs* tetragonal. Furthermore, a more pronounced phase transition from tetragonal to cubic structure is observed in the DSC and in situ WAX data. A pronounced crystal expansion in nitrogen annealed perovskite for 5 h could arise from the increased fraction of tetragonal phase in the tetragonal–pseudocubic phase of the perovskite.

On the other hand a stark crystal contraction observed when annealed in air for 5 h could originate by

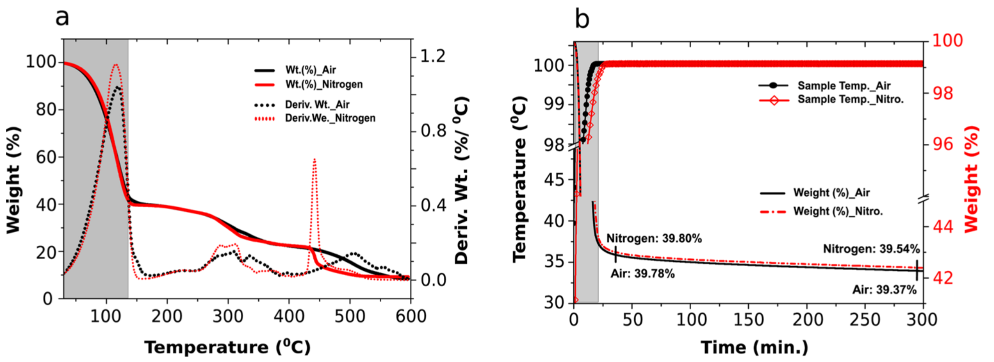

Figure 5. (a) TGA profiles of perovkite precursor solution heated up to 600 °C in 10 °C/min. (b) DSC and TGA response of perovskite while annealing isothermally at 100 °C. Shaded area indicates the formation of perovskite crystals from a precursor solution and evaporation of the solvent.

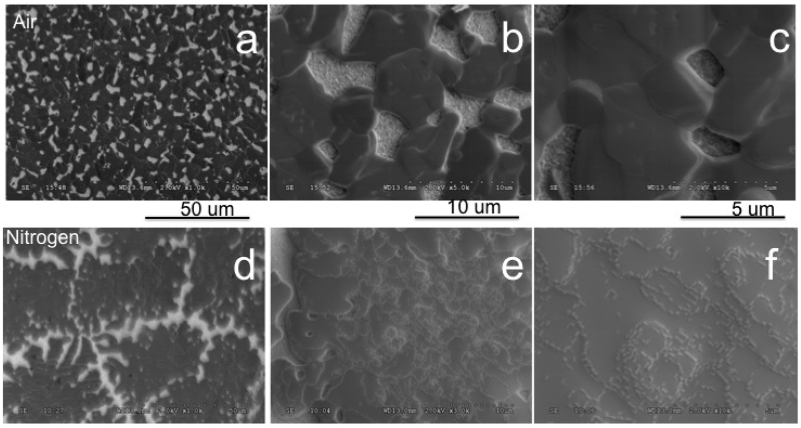

Figure 6. SEM image of perovskite films. (a and d) Annealed for 1 h in air and nitrogen, respectively. Annealing in nitrogen produces a perovskite film with better surface coverage but with smaller grain size, contrary to what is observed when annealed in air. (b and e) Annealed for 5 h in air and nitrogen, respectively. (c and f) The magnified version of b and e, respectively. Longer annealing (*e.g.*, 5 h) time in nitrogen atmosphere generates secondary grains with much smaller size; no such secondary process is observed in air even after 5 h of annealing.

retaining higher fraction of cubic phase in the perovskite crystal when cooled to room temperature (the cubic crystal structure has a smaller cell volume compared to tetragonal one).

It is also important to investigate whether such a variation in photophysical properties are originated due to the structural deterioration while annealing, we have performed differential scanning calorimetry (DSC) up to 600 °C and thermogravimetric analyze (TGA) annealed (up to 5 h) at 100 °C, in nitrogen and air atmospheres for bulk perovskite samples, as shown in Figure 5 a and b.

We observe no identifiable change in the sample temperature profiles in both air and nitrogen atmosphere hence no evidence for structural degradation in isothermal TGA curves or any other processes occurring while samples are isothermally annealed at 100 °C. Two clear observations can be made by the TGA data: First, the byproduct of the perovskite synthesis, *i.e.*, two CH_3NH_3X (X = Cl/or I), may not have completely evaporated off during the annealing process, leaving behind the solid solution of excess by products (CH_3NH_3X where X = Cl/or I)) in the film itself. Second, degradation kinetics is influenced by the surrounding atmosphere; when annealed in nitrogen, a faster degradation is observed as compared with air annealing where a slower and delayed degradation is seen. A sharp and prior degradation of CH_3NH_3X (X = Cl/or I) at around 300 °C and PbX_2 (X = Cl/or I) at around 400–500 °C is clearly visible in nitrogen atmosphere, which is slightly delayed in the case of air annealing indicate a slower degradation mechanism.

We investigated the variation in the microstructural features of the perovskite film when annealed under different atmosphere by means of SEM, as shown in Figure 6. Figure 6a and d show SEM image of perovskite annealed for 1 h in air and nitrogen, respectively. SEM image of a perovskite film annealed in nitrogen atmosphere shows a larger surface coverage compared to air annealed sample. Interestingly, the perovskite grain domains are much smaller when annealed in nitrogen atmosphere whereas, large and more defined crystal grain domains are observed in air annealed samples. Further annealing for longer time for up to

5 h in air did not produce any remarkable difference in microstructure of grains as shown in Figure 6b and c. In contrast annealing in nitrogen for longer period (*i.e.*, 2.5 and 5 h) shows nucleation of tiny secondary grains formed on the surface of microcrystallites and the grain boundaries. These tiny grains grow in number with increasing dwell time. An SEM image of a perovskite film annealed for 5 h in nitrogen is shown in Figure 6e as much smaller and brighter needle shape secondary grains can be seen throughout the film. Atmospheric influence on the perovskite microstructural features can be understood by the considering the different in the kinetics of the crystallization (*i.e.*, forming grain boundaries, grain boundary movement and neck formation). The perovskite crystallization is both driven by thermodynamic as well as kintetic process, observed in TGA and DSC measurements (see Figure 5); annealing in nitrogen atmosphere induces faster crystallization of the perovskite on the substrate, whereas in air, a slower crystallization is observed. When perovskite precursor is spin coated in nitrogen atmosphere many nucleation centers are generated due to faster solvent removal, which by subsequent annealing will form many small grains. The higher density of nucleation centers across the film produces larger surface coverage but smaller grain domains. On the other hand, when annealed in air atmosphere crystallization process is relatively slower ensuring fewer numbers of nucleation canters and allowing enough time for coarsening of the nucleated grains, resulting into a large grain domain.[41] The electron probe microanalysis (EPMA) on the small grains that appears in the perovskite film when annealed for longer period (*i.e.*, 2.5 and 5 h) shows elemental ratio Pb:I 1:3 confirming the formation of the perovskite. The contrast difference in photophysical properties of the perovskite films annealed in different atmosphere is result of a difference in the degree of electronic disorder in the film. Lower PLQE, shorter PL lifetime and higher Urbach energy clearly indicate toward higher electronic disorder in the nitrogen annealed perovskite. Now the question is to identify the origin of such electronic disorder in the film. Our extensive investigation on the variation in the crystallographic parameter and microstructure indicate toward a complex scenario where several factors are of importance. However, to our understanding, it appears that changes occur on a macroscopic level (*i.e.*, difference in grain domain size) may be the dominant at least up to 1 h of annealing. Smaller grain domains means higher density of grain boundaries in the film, higher density of grain boundary inducing higher number of electronic trap states.

On the contrary, larger grain domain assures lower electronic traps in the film. Further annealing in nitrogen makes the perovskite having smaller secondary grains forming at the grain boundaries and deterioration of the crystallinity that further lowers performance. On the contrary, no such deterioration is encountered when the samples were annealed in air for even 5 h, and this correlates with the observed higher PLQE, longer PL decay time and lower Urbach energy. Further increasing the annealing time in nitrogen atmosphere generates secondary grains with much smaller size, on the other hand in air atmosphere no such deterioration is observed.

Yang Yang *et al.*[42] have recently reported the self-induced PbI_2 in the perovskite film while annealing in air and its influence on device performance; however, a detailed mechanism for crystallization process was not discussed. The work here helps to explain these exceptionally high efficiencies.[42]

The other major source of defect states in perovskite during annealing, other than different crystal structures and variation in perovskite grain domain size, could arise from nonstoichiometric point defects in perovskite films. Oxygen molecules may act as a passivation agent to those defects. To avoid the contribution from nonstoichiometric defects we exposed the nitrogen annealed films to air overnight, to try and ensure that the differences we are observing are predominantly from the variation in crystal structure induced during crystallization. Investigation on the nonstoichiometric point defects shall be studied separately. This study also open up another questions whether varying annealing conditions influences the extent of chloride doping in the perovskite crystal.

CONCLUSIONS

We have investigated the influence of annealing conditions on the photophysical properties of perovskite films and correlated this with the annealing induced variations in the perovskite crystal structure. We observed that limiting nonradiative pathways (*i.e.*, maximizing PLQE) is important for obtaining the highest device efficiency. The perovskite films annealed in nitrogen atmosphere have higher degree of electronic disorder than their air-annealed counterparts, as evident in the measured Urbach energy. The higher degree of disorder leads to lower value of PLQE, shorter PL lifetime and hence lower device performance as compared with air annealed samples, which show much lower level of disorder. The degree of disorder increases gradually with the dwelling time (2.5 and 5 h) in nitrogen atmosphere, in contrast with air-annealing where no substantial variation in device performance is observed.

Under similar conditions we investigated the change in perovskite crystal structure by XRD and *in situ* WAX measurements; we also investigated the microstructure of the perovskite film under stated conditions. Several factors including crystallographic changes, oxygen passivation and variation in grain domain size may play a composite role in deciding the influence of atmosphere while annealing on the photophysical properties of the perovskite. However, we believe that variation in the macroscopic property, *i.e.*, grain size, may play a predominant role on this. Perovskite with larger grain size should have lesser electronic trap states as compared with the smaller ones. Perovskite film with even larger grain domain without compromising the surface coverage should realize the PCE >20% in perovskite solar cell.

EXPERIMENTAL SECTION

A DMF solution of methyl-ammonium iodide (MAI) and $PbCl_2$ (3:1 molar ratio) was mixed to form perovskite precursor solution as described elsewhere.[20] The precursor solution was then deposited by spin coating in glovebox (nitrogen atmosphere) and in air and annealed under the same conditions at 100 C for 1, 2.5, and 5 h. WAXS measurements were conducted on bulk perovskite powder obtained from scraping off the spin-coted perovskite films. For UV, PL measurements perovskite was spin-coated on clean and plasma etched glass slides.

In situ WAXS was performed at beamline I22, at the Diamond Light Source at the Harwell Science and Innovation Campus in Didcot, U.K. The energy was set at $E = 8$ keV. The beam was focused to a size of 200×100 μm^2 at the sample position. A Pilatus 300k detector with a pixel size of 172 μm^2 was used for WAXS with a sample–detector distance of 0.4 m. The measuring time was 15 s for all the measurements. The samples were moved out of the beam after each measurement to avoid beam damage. The *q*-space calibration was performed fitting the characteristic scattering signal arising from silver behenate. The construction of 1D profiles and the modeling of the crystal structure were carried out using the self-written GISAS analysis package (http://steiner.bss.phy.cam.ac.uk/facilities/sas-gisas-analysis-package).

X-ray diffraction was measured using Bruker D8 theta/theta (*i.e.*, fixed sample) spectrometer with a position sensitive detector (LynxEye) and a standard detector (SC) with autoabsorber and graphite second beam monochromator. (Bragg–Brentano parafocusing geometry, reflection mode). UV–vis absorption was measured on films in air using a commercial spectrophotometer (Varian Cary 300 UV- Vis, USA). Time-resolved PL measurements were acquired using a time correlated single photon counting (TCSPC) setup (FluoTime 300, PicoQuant GmbH). Film samples were photoexcited using a 507 nm laser head (LDH–P-C-510, PicoQuant GmbH) pulsed at frequencies of 1 MHz, with a pulse duration of 117 ps and fluence of ∼300 nJ/cm2. The PL was collected using a high resolution monochromator and hybrid photomultiplier detector assembly (PMA Hybrid 40, PicoQuant GmbH).

PDS samples were prepared on 13 mm quartz substrates in the said conditions. In PDS measurements, the sample was exposed to monochromatic light (pump beam), producing a thermal gradient due to the nonradiative relaxation of the absorbed light. This results in a refractive index gradient in the area surrounding the sample surface, which is further enhanced by immersing the sample in an inert liquid (Fluorinert FC-72), which has high refractive index changes for small variations in temperature. A fixed wavelength continuous wave laser beam (probe beam) (670 nm) was passed through this refractive index gradient producing a deflection proportional to the absorbed light. This deflection is measured using a position sensing detector and a lock-in amplifier. The deflection is proportional to the light absorbed by the sample at that given wavelength of the pump beam, and scanning through the wavelengths yields a complete absorption spectrum.

Q2000 differential scanning calorimeter was used to measure the heat flow during the reaction. Samples contained in open aluminum pans and heated at 10 °C/min to 100 °C. Nitrogen and air gas was purge with 20 cc/min flow rate. To evaluate the weight loss during the annealing Q500 Thermo gravimetric analyzer was used, samples were placed in aluminum pan under the air/nitrogen purge (20 cc/min flow rate), and weight loss was measured over the 5 h hold period at 100 °C.

Solar cells were constructed as discussed before.[43] Briefly, FTO-coated glass sheets (7/□, Pilkington) were etched with zinc powder and HCl (2M) to obtain the required electrode pattern. The sheets were then washed with soap (2% Hellmanex in water), deionized water, acetone, and methanol. The last traces of organic residues were removed by oxygen plasma cleaning. The FTO sheets were subsequently coated with a compact layer of TiO_2 (100 nm) by spin-coating titanium sol precursor at 2000 rpm. The titanium precursor sol was prepared by dropwise adding a solution of 175 μL of Ti isopropoxide in 1.25 mL of EtOH into a solution of 17.5 μL of 2 M HCl in 1.25 mL of EtOH. The coated FTO substrate was then heated to 300 °C for 30 min. An Al_2O_3 meso-structured scaffold was deposited by spin-coating a colloidal dispersion of 20 nm Al_2O_3 nanoparticles in isopropanol, followed by drying at 150 °C. Upon cooling to room temperature, perovskite precursor solution was deposited by spin-coating, which forms a perovskite after heating to 100 °C for 1, 2.5, and 5 h under different atmosphere (air and glovebox). Spiro-MeOTAD (LUMTECH) hole-conductor at 2000 rpm for 60 s in air. The solution for spin-coating consisted of spiro-MeOTAD dissolved in anhydrous chlorobenzene (reagent grade) at 10 vol %, assuming a density of spiro-MeOTAD of 1 g cm^{-3}. *tert*-Butylpyridine (tbp) was added to the solution at a concentration of 1.26 $\mu L\ mg^{-1}$ (tbp: spiro-OMeTAD). Lithium bis-(trifluoromethyl sulfonyl)imide salt (Li-TFSI) (170 mg mL^{-1} in acetonitrile) was added. After drying overnight, back contacts were applied by thermal evaporation of 150 nm of silver.

Solar-cell performance parameters were measured using solar-simulated AM 1.5 sunlight was generated with an ABET solar simulator calibrated to output 100 mW cm^{-2} using an NREL- calibrated KG5 filtered silicon reference cell, and the *J*–*V* curves were recorded with a Keithley 2400 source meter. The solar cells were masked with a metal aperture defining an active area of 0.09 cm^2. For TA a measurement the device was held at open-circuit in a nitrogen filled holder and was photoexcited at 2.33 eV (10 μJ/cm, pulse length 400 ps). Excitation fluence for films was 2 $\mu J/cm^2$.

Conflict of Interest: The authors declare no competing financial interest.

Acknowledgment. We thank Diamond Light Source for access to beamline I22 (SM8459) that contributed to the results presented here. We thank P. Staniec, S.-H. Liu, X. Sheng, M. Scherer and N. Terrill for their help during the I22 experiment.

Supporting Information Available: Supporting figures (Figure S1–S5). This material is available free of charge *via* the Internet at http://pubs.acs.org.

REFERENCES AND NOTES

1. Chu, S.; Majumdar, A. Opportunities and Challenges for a Sustainable Energy Future. *Nature* **2012**, *488*, 294–303.
2. O'regan, B.; Grätzel, M. A Low-Cost, High Efficiency Solar Cell Based on Dye-Sensirized Colloidal TiO_2 Films. *Nature* **1991**, *353*, 737–740.
3. Janssen, R. a J.; Nelson, J. Factors Limiting Device Efficiency in Organic Photovoltaics. *Adv. Mater.* **2013**, *25*, 1847–1858.
4. Todorov, T.; Mitzi, D. B. Direct Liquid Coating of Chalcopyrite Light-Absorbing Layers for Photovoltaic Devices. *Eur. J. Inorg. Chem.* **2010**, *2010*, 17–28.
5. Sargent, E. H. Colloidal Quantum Dot Solar Cells. *Nat. Photonics* **2012**, *6*, 133–135.
6. Lim, C.-S.; Im, S. H.; Rhee, J. H.; Lee, Y. H.; Kim, H.-J.; Maiti, N.; Kang, Y.; Chang, J. A.; Nazeeruddin, M. K.; Grätzel, M.; *et al.*

Hole-Conducting Mediator for Stable Sb_2S_3-Sensitized Photoelectrochemical Solar Cells. *J. Mater. Chem.* **2012**, *22*, 1107–1111.

7. Graetzel, M.; Janssen, R. a J.; Mitzi, D. B.; Sargent, E. H. Materials Interface Engineering for Solution-Processed Photovoltaics. *Nature* **2012**, *488*, 304–312.
8. Hodes, G.; Cahen, D. All-Solid-State, Semiconductor-Sensitized Nanoporous Solar Cells. *Acc. Chem. Res.* **2012**, *45*, 705–713.
9. Yu, G.; Gao, J.; Hummelen, J. C.; Wudl, F.; Heeger, A. J. Polymer Photovoltaic Cells: Enhanced Efficiencies *via* a Network of Internal Donor-Acceptor Heterojunctions. *Science* **1995**, *270*, 1789–1791.
10. Halls, J.; Walsh, C.; Greenham, N.; Marseglia, E.; Friend, R.; Moratti, S.; Holmes, A. Efficient Photodiodes from Interpenetrating Polymer Networks. *Nature* **1995**, *376*, 498–500.
11. Chung, I.; Lee, B.; He, J.; Chang, R. P. H.; Kanatzidis, M. G. All-Solid-State Dye-Sensitized Solar Cells with High Efficiency. *Nature* **2012**, *485*, 486–489.
12. Ball, J. M.; Lee, M. M.; Hey, A.; Snaith, H. J. Low-Temperature Processed Meso-Superstructured to Thin-Film Perovskite Solar Cells. *Energy Environ. Sci.* **2013**, *6*, 1739–1743.
13. Heo, J. H.; Im, S. H.; Noh, J. H.; Mandal, T. N.; Lim, C.; Chang, J. A.; Lee, Y. H.; Kim, H.; Sarkar, A.; Nazeeruddin, K.; *et al.* Efficient Inorganic-Organic Hybrid Heterojunction Solar Cells Containing Perovskite Compound and Polymeric Hole Conductors. *Nat. Photonics* **2013**, *7*, 1–6.
14. Kim, H.-S.; Lee, C.-R.; Im, J.-H.; Lee, K.-B.; Moehl, T.; Marchioro, A.; Moon, S.-J.; Humphry-Baker, R.; Yum, J.-H.; Moser, J. E.; *et al.* Lead Iodide Perovskite Sensitized All-Solid-State Submicron Thin Film Mesoscopic Solar Cell with Efficiency Exceeding 9%. *Sci. Rep.* **2012**, *2*, 591–598.
15. Liu, M.; Johnston, M. B.; Snaith, H. J. Efficient Planar Heterojunction Perovskite Solar Cells by Vapour Deposition. *Nature* **2013**, *501*, 395–398.
16. Burschka, J.; Pellet, N.; Moon, S.-J.; Humphry-Baker, R.; Gao, P.; Nazeeruddin, M. K.; Grätzel, M. Sequential Deposition as a Route to High-Performance Perovskite-Sensitized Solar Cells. *Nature* **2013**, *499*, 316–319.
17. Kojima, A.; Teshima, K.; Shirai, Y.; Miyasaka, T. Organometal Halide Perovskites as Visible-Light Sensitizers for Photovoltaic Cells. *J. Am. Chem. Soc.* **2009**, *131*, 6050–6051.
18. Mitzi, D. B. Synthesis, Structure, and Properties of Organic−Inorganic Perovskites and Related Materials. In *Progress in Inorganic Chemistry*; John Wiley & Sons, Inc.: New York, 2007; pp 1−121.
19. Wasylishen, E.; White, M. A.; Stanley, T.; Michiel, J. M. Alkylammonium Lead Halides. Part 2. $CH_3NH_3PbX_3$ (X = C1, Br, I) Perovskites: Cuboctahedral Halide Cages with Isotropic Cation reorientation1. *Can. J. Chem.* **1990**, *68*, 412–422.
20. Lee, M. M.; Teuscher, J.; Miyasaka, T.; Murakami, T. N.; Snaith, H. J. Efficient Hybrid Solar Cells Based on Meso-Superstructured Organometal Halide Perovskites. *Science* **2012**, *338*, 643–647.
21. Stranks, S. D.; Eperon, G. E.; Grancini, G.; Menelaou, C.; Alcocer, M. J. P.; Leijtens, T.; Herz, L. M.; Petrozza, A.; Snaith, H. J. Electron-Hole Diffusion Lengths Exceeding 1 Micrometer in an Organometal Trihalide Perovskite Absorber. *Science* **2013**, *342*, 341–344.
22. Xing, G.; Mathews, N.; Sun, S.; Lim, S. S.; Lam, Y. M.; Grätzel, M.; Mhaisalkar, S.; Sum, T. C. Long-Range Balanced Electron- and Hole-Transport Lengths in Organic-Inorganic $CH_3NH_3PbI_3$. *Science* **2013**, *342*, 344–347.
23. Edri, E.; Kirmayer, S.; Mukhopadhyay, S.; Gartsman, K.; Hodes, G.; Cahen, D. Elucidating the Charge Carrier Separation and Working Mechanism of $CH_3NH_3PbI_{3-x}Cl_x$ Perovskite Solar Cells. *Nat. Commun.* **2014**, *5*, 3461–3469.
24. Wehrenfennig, C.; Eperon, G. E.; Johnston, M. B.; Snaith, H. J.; Herz, L. M. High Charge Carrier Mobilities and Lifetimes in Organolead Trihalide Perovskites. *Adv. Mater.* **2014**, *26*, 1584–1589.
25. Deschler, F.; Price, M.; Pathak, S.; Klintberg, L.; Jarausch, D. D.; Higler, R.; Huettner, S.; Leijtens, T.; Stranks, S. D.; Snaith, H. J.; *et al.* High Photoluminescence Efficiency and Optically-Pumped Lasing in Solution-Processed Mixed Halide Perovskite Semiconductors. *J. Phys. Chem. Lett.* **2014**, *5*, 1421–1426.
26. Kawamura, Y.; Mashiyama, H.; Hasebe, K. Structural Study on Cubic−Tetragonal Transition of $CH_3NH_3PbI_3$. *J. Phys. Soc. Jpn.* **2002**, *71*, 1694–1697.
27. Takahashi, Y.; Obara, R.; Lin, Z.-Z.; Takahashi, Y.; Naito, T.; Inabe, T.; Ishibashi, S.; Terakura, K. Charge-Transport in Tin-Iodide Perovskite $CH_3NH_3SnI_3$: Origin of High Conductivity. *Dalton Trans.* **2011**, *40*, 5563–5568.
28. Li, Y.; Zheng, G.; Lin, C.; Lin, J. New Organic−Inorganic Perovskite Materials with Different Optical Properties Modulated by Different Inorganic Sheets. *Cryst. Growth Des.* **2008**, *8*, 1990–1996.
29. Sirringhaus, H. Device Physics of Solution-Processed Organic Field-Effect Transistors. *Adv. Mater.* **2005**, *17*, 2411–2425.
30. Mosconi, E.; Amat, A.; Nazeeruddin, K.; Gra, M.; De Angelis, F. First-Principles Modeling of Mixed Halide Organometal Perovskites for Photovoltaic Applications. *J. Phys. Chem. C* **2013**, *117*, 13902–13913.
31. Baikie, T.; Fang, Y.; Kadro, J. M.; Schreyer, M.; Wei, F.; Mhaisalkar, S. G.; Graetzel, M.; White, T. J. Synthesis and Crystal Chemistry of the Hybrid Perovskite $(CH_3NH_3)PbI_3$ for Solid-State Sensitised Solar Cell Applications. *J. Mater. Chem. A* **2013**, *1*, 5628–5641.
32. Leite, E. R.; Nascimento, A. M.; Bueno, P. R.; Longo, E.; Sa, U. F.; De Carlos, A.; Box, P. O.; Carlos, A. The Infuence of Sintering Process and Atmosphere on the Non-Ohmic Properties of SnO_2 Based Varistor. *J. Mater. Sci.: Mater. Electron.* **1999**, *10*, 321–327.
33. Nanova, D.; Kast, A. K.; Pfannmöller, M.; Müller, C.; Veith, L.; Wacker, I.; Agari, M.; Hermes, W.; Erk, P.; Kowalsky, W.; *et al.* Unraveling the Nanoscale Morphologies of Mesoporous Perovskite Solar Cells and Their Correlation to Device Performance. *Nano Lett.* **2014**, *14*, 2735–2740.
34. Snaith, H. J.; Abate, A.; Ball, J. M.; Eperon, G. E.; Leijtens, T.; Noel, N. K.; Stranks, S. D.; Wang, J. T.; Wojciechowski, K.; Zhang, W. Anomalous Hysteresis in Perovskite Solar Cells. *J. Phys. Chem. Lett.* **2014**, *17*, 1511–1515.
35. De Bastiani, M.; D'Innocenzo, V.; Stranks, S. D.; Snaith, H. J.; Petrozza, A. Role of the Crystallization Substrate on the Photoluminescence Properties of Organo-Lead Mixed Halides Perovskites. *APL Mater.* **2014**, *2*, 81509–81515.
36. Rau, U. Reciprocity Relation between Photovoltaic Quantum Efficiency and Electroluminescent Emission of Solar Cells. *Phys. Rev. B: Condens. Matter Mater. Phys.* **2007**, *76*, 85303.
37. Miller, O. D.; Yablonovitch, E.; Kurtz, S. R. Strong Internal and External Luminescence as Solar Cells Approach the Shockley−Queisser Limit. *IEEE J. Photovoltaics* **2012**, *2*, 303–311.
38. Bezryadina, a.; France, C.; Graham, R.; Yang, L.; Carter, S. a.; Alers, G. B. Mid-Gap Trap States in CdTe Nanoparticle Solar Cells. *Appl. Phys. Lett.* **2012**, *100*, 013508–013513.
39. Sadhanala, A.; Deschler, F.; Thomas, T. H.; Dutton, S. E.; Goedel, K. C.; Hanusch, F. C.; Lai, M. L.; Steiner, U.; Bein, T.; Docampo, P.; *et al.* Preparation of Single-Phase Films of $CH_3NH_3Pb(I_{1-x}Br_x)_3$ with Sharp Optical Band Edges. *J. Phys. Chem. Lett.* **2014**, *5*, 2501–2505.
40. De Wolf, S.; Holovsky, J.; Moon, S.-J.; Löper, P.; Niesen, B.; Ledinsky, M.; Haug, F.-J.; Yum, J.-H.; Ballif, C. Organometallic Halide Perovskites: Sharp Optical Absorption Edge and Its Relation to Photovoltaic Performance. *J. Phys. Chem. Lett.* **2014**, *5*, 1035–1039.
41. Exner, H. E.; Müller, C. Particle Rearrangement and Pore Space Coarsening During Solid-State Sintering. *J. Am. Ceram. Soc.* **2009**, *92*, 1384–1390.
42. Chen, Q.; Zhou, H.; Song, T.-B.; Luo, S.; Hong, Z.; Duan, H.-S.; Dou, L.; Liu, Y.; Yang, Y. Controllable Self-Induced Passivation of Hybrid Lead Iodide Perovskites toward High Performance Solar Cells. *Nano Lett.* **2014**, *14*, 4158–4163.
43. Ball, J. M.; Lee, M. M.; Hey, A.; Snaith, H. J. Low-Temperature Processed Meso-Superstructured to Thin-Film Perovskite Solar Cells. *Energy Environ. Sci.* **2013**, *6*, 1739–1743.